

Transparent Shape from Single Polarization Images

Mingqi Shao, Chongkun Xia, Zhendong Yang, Junnan Huang, and Xueqian Wang

Tsinghua Shenzhen International Graduate School
{smq21,yangzd21,hjn21}@mails.tsinghua.edu.cn
{xiachongkun,wang.xq}@sz.tsinghua.edu.cn

Abstract. This paper presents a data-driven approach for transparent shape from polarization. Due to the inherent high transmittance, the previous shape from polarization(SfP) methods based on specular reflection model have difficulty in estimating transparent shape, and the lack of datasets for transparent SfP also limits the application of the data-driven approach. Hence, we construct the transparent SfP dataset which consists of both synthetic and real-world datasets. To determine the reliability of the physics-based reflection model, we define the physics-based prior confidence by exploiting the inherent fault of polarization information, then we propose a multi-branch fusion network to embed the confidence. Experimental results show that our approach outperforms other SfP methods. Compared with the previous method, the mean and median angular error of our approach are reduced from 19.00° and 14.91° to 16.72° and 13.36° , and the accuracy $11.25^\circ, 22.5^\circ, 30^\circ$ are improved from 38.36%, 77.36%, 87.48% to 45.51%, 78.86%, 89.98%, respectively. Our dataset and code will be publicly available at <https://github.com/shaomq2187/TransSfP>.

Keywords: Shape from Polarization, Transparent Object, Deep Learning

1 Introduction

Surface normals provide detailed 3D information about the surface of objects, hence the estimation of surface normals is an active research topic in computer vision. Photometric information can help recover per-pixel surface normal from images, such as shape from shading[12], photometric stereo[4], these are typical photometric 3D reconstruction methods. These algorithms that perform well on opaque objects, however, can not be directly applied to transparent objects because of the complex reflection and refraction between transparent objects and light.

In this paper, we focus on estimating surface normals of transparent objects from a single polarization image. Compared with shape from shading and photometric stereo, SfP can establish the relationship between the surface polarization

information of transparent object and its surface geometry. In particular, the commercial polarization image sensors[34] appeared in recent years have made it possible to capture polarization images at a single shot, making the acquisition of polarization images more relaxed than other photometric methods.

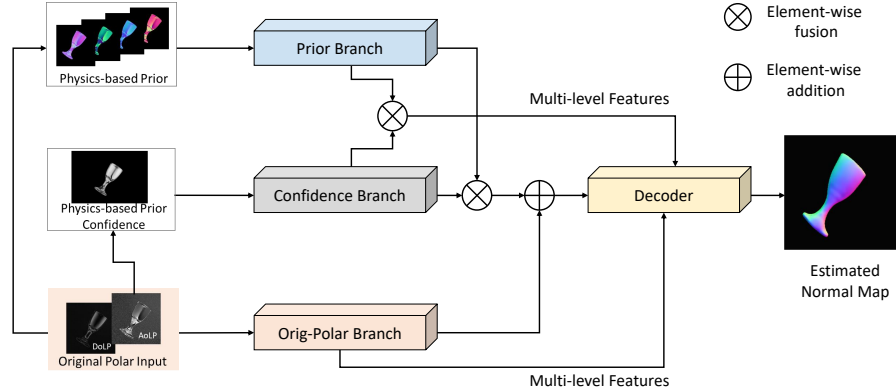


Fig. 1. Overview of our proposed method. We use a multi-encoders architecture to handle different information and define the physics-based prior confidence by using the angle of linear polarization(AoLP). The confidence map is used for weighted fusion of the original polar input and physical prior input at the multi-levels

However, there are still challenges in using polarization information to estimate the surface normals of transparent objects. Firstly, there are two physical models that can estimate the surface normals from polarization state, the specular polarization model(will describe in Section 3.1) and the diffuse polarization model. For smooth objects such as glass, the specular reflection is dominant in the surface reflection component. However, due to the high transmittance of transparent objects, the specular reflection energy only accounts for about 4% of the incident light energy[44], the interference from the transmitted background is superimposed on the observed polarization information, leading to the high estimation error of the physics-based SfP methods. Secondly, in recent years, some works have tried to use deep learning to solve the SfP problem[2, 3, 8, 16, 17], and corresponding datasets have also been proposed, such as deepSfP dataset[3], SPW dataset[17]. But to the best of our knowledge, there are no public accessible transparent object polarization datasets, which limits the application of data-driven methods to the transparent SfP problem.

To address the challenge of the lack of transparent object polarization dataset, we build the dataset TransSfP for transparent shape from polarization. Aiming at the problem that the reliability of the Fresnel physical model is reduced due to the complex interaction of light in transparent objects, we propose the concept of physics-based prior confidence to perform a weighted fusion of the original polarization input and the physical prior. As shown in Fig.1, the network architecture

of multiple encoders is used to extract features of the original polarization input and physics-based prior. We note that areas with higher transmittance will have more noise from the background in the AoLP map, this characteristic is utilized to define the concept of physics-based prior confidence to determine the contribution of the physical prior. We summarize our contributions as follows:

1. We established the TransSfP dataset for transparent shape from polarization, which contains both synthetic dataset and real-world dataset.
2. We utilized the intrinsic fault of polarization observation to define the concept of physical prior confidence, which is used as prior attention map for physics-based prior.
3. Our proposed multi-branch fusion network is designed to address the transparent SfP problem and achieves the best-performing results on the TransSfP dataset. Our work provides a new view for further transparent SfP research.

2 Related Work

2.1 Shape from Polarization

When a beam of unpolarized incident light is reflected from the surface of an object, the polarization state of the light will change according to the incident angle, the relative refractive index, and the surface normal vector of the surface. This process can be quantitatively described by Fresnel equations[1]. Therefore, by observing the polarization state, the surface normal encoded in it can be obtained. Fresnel equations tell us that the polarization state corresponds to multiple surface orientations, which is the well-known ambiguity in SfP[1]. Early works relied on the physical model of Fresnel equations to recover surface normals. Due to the inherent ambiguity of SfP, other constraints were required to determine a unique surface normal, including rotation measurements[26], active lighting[30, 31, 29], boundary prior[28], shading cues[23], but these methods are limited due to strict assumptions.

In addition to the inherent ambiguity, the classical SfP using the physical model of Fresnel equations also has disadvantages such as refraction distortion, Fronto-parallel surface, depth discontinuity, and relative depth[39]. These problems can be solved by integrating SfP with other methods. Combining SfP with methods that can provide coarse geometric cues can resolve the ambiguity and relative depth problems. Fukao et al.[11] recovered complex non-Lambertian surface using a pair of polarimetric cameras. Cui et al.[7] generated an initial depth map from multi-view polarimetric images and then optimized the details of the initial depth map with polarization information. Yang et al.[48] introduced polarization information into SLAM and implemented a real-time polarization 3D reconstruction system. The depth sensor can directly provide the initial depth map, some works tried to combine the depth sensor with SfP to obtain high-quality reconstruction results[13, 14, 52, 43].

With the vigorous development of deep learning in many areas of computer vision, the combination of SfP and deep learning has attracted the attention of researchers. Ba et al.[3] first proposed using deep learning to solve the SfP problem and established a real-world object-level dataset. Deschaintre et al.[8] built a dataset and constructed a network capable of predicting objects' shape and SVBRDF. Some works extended 'Sfp + deep learning' to other tasks, such as scene-level normal estimation[17], human body shape estimation[55, 56]. However, these approaches and datasets all focus on opaque objects. As far as we know, there are no publicly available polarization datasets and deep learning models for transparent objects. To address this issue, we propose the first dataset and deep learning model for transparent shape from polarization.

2.2 Shape Estimation for Transparent Objects

Shape estimation for transparent objects is a challenging problem[47]. Active lighting and capture devices are used in many methods to estimate the shape of transparent objects, such as shape from the distortion of the calibration pattern by transparent objects[45, 41], shape from the reflection of transparent objects to known ambient light[32, 49], shape from heated transparent objects by using infrared light[9], shape from the corresponding relationship between the incident and reflected light[47, 21]. These methods all require expensive experimental equipment and tedious reconstruction steps. Some researchers tried to use cheaper devices to estimate the surface shape of transparent objects. Yeung et al.[50] tried to recover the transparent surface normal from a video. Zhu et al.[54] used a RGB-D sensor and built a SLAM system 'TransFusion' for transparent object. Li et al.[20] employed multi-view RGB images to reconstruct transparent shape. There are also some works focusing on RGB-D sensor depth completion[38, 53, 42, 10], which can complete the depth map of scenes containing transparent objects from a single view.

As a method with advantages of single-view, weak assumption of lighting and passive imaging, shape from polarization has long been used to estimate the surface of transparent objects. Saito et al.[37] applied Fresnels's law to solve surface orientation by measuring the polarization information of the transparent object in an optical diffuser. In order to solve the ambiguity in SfP, Miyazaki et al.[27] proposed a method of rotating the transparent object with a tiny angle and matching the feature points of the two polarization states. Since the polarization state of transparent objects is seriously affected by internal reflection, refraction and transmission, Miyazaki et al.[24, 25] employed inverse raytracing to optimize transparent shapes. Liu et al.[22] overcame the limitations of paraxial assumption and s-component approximation assumption in polarization imaging for transparent surface by using vector operations. Different from these works that the research objects are simple transparent spheres and plates, we hope to estimate surface shape for complex transparent objects by combining SfP with deep learning.

3 Method

3.1 Physics-based Prior for Transparent Shape from Polarization

When a polarizer is placed in front of the camera at a specific angle θ_{pol} , the brightness of the pixels observed by the camera will vary with θ_{pol} according to a sinusoid function:

$$I(\theta_{pol}, \phi) = \frac{I_{max} + I_{min}}{2} [1 + \rho \cos(2\theta_{pol} - 2\phi)] \quad (1)$$

where I_{max} and I_{min} are the maximum and minimum intensity measured within θ_{pol} rotate from 0 to π . ρ and ϕ are the degree of linear polarization(DoLP) and angle of linear polarization(AoLP) respectively since only linear polarization is considered in this paper. DoLP represents the ratio of the light intensity of the polarized part to the total light intensity, which can be defined as:

$$\rho = \frac{I_{max} - I_{min}}{I_{max} + I_{min}} \quad (2)$$

By observing the light intensity at least 3 different θ_{pol} , the polarization information of each pixel can be obtained, including intensity map, DoLP map, AoLP map. Different reflection types have different polarization states[46]. When the specular reflection is dominant, the DoLP can be written as follows given zenith angle θ and refraction index n by using Fresnel equations[1]:

$$\rho = \frac{2 \sin^2 \theta \cos \theta \sqrt{n^2 - \sin^2 \theta}}{n^2 - \sin^2 \theta - n^2 \sin^2 \theta + 2 \sin^4 \theta} \quad (3)$$

The above equation shows that two zenith angles can be determined for a given DoLP and the ambiguous solution can not be ruled out without other auxiliary information. Apart from the ambiguity of the zenith angle, the azimuth angle solution is also ambiguous. When the specular reflection is dominant, the azimuth angle φ differs from the AoLP ϕ by $\frac{\pi}{2}$, i.e.

$$\varphi = \phi \pm \frac{\pi}{2} \quad (4)$$

Obviously, the azimuth angle also has two solutions with a difference of π , which is called **π -ambiguity**[3]. The π -ambiguity of the azimuth angle derives from the period of the sinusoid function in Eq.1. There is also **$\frac{\pi}{2}$ -ambiguity** due to the uncertainty of specular and diffuse reflections[1], but it is not considered in this paper since the diffuse reflection component of the smooth surface of transparent objects can be ignored[27].

Similar to the method in deepSfP[3], we employ the Fresnel specular reflection physical model, Eq.3 and Eq.4 with $n = 1.52$, to calculate four normal maps as physics-based prior. The difference is the polarization information of transparent objects is severely interfered with internal refraction, transmission [25], hence in addition to overcoming the ambiguity of physics-based prior, its reliability should also be determined.

3.2 Physics-based Prior Confidence

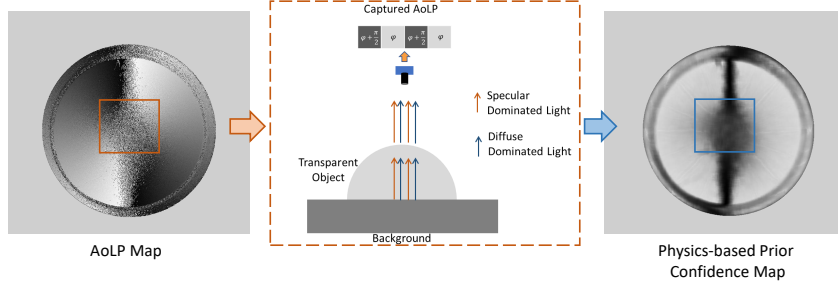


Fig. 2. The intrinsic fault in the AoLP map of transparent objects is used to define the physics-based prior confidence. The schematic diagram in the middle shows that the noise in the box in the AoLP map is derived from the transition between specular dominance and diffuse dominance

The high transmittance of transparent objects is an obstacle to normal estimation using the SfP method. When the transmittance is large, most of the light captured by the camera comes from the background, and the specular light, which contains information about the surface normal, is tiny. Using the physics-based prior in the areas with large transmittance will lead to a large angular error, therefore, the transmittance of each area needs to be determined for flexible use of physics-based prior.

By observing the AoLP maps of transparent objects, we found that the area with higher transmittance will contain more noise from the background. As shown in Fig.2, at the center of the transparent hemisphere, most of the observed light comes from the background since the zenith angle is close to 0. Due to the non-smooth material, the background has both specular reflection and diffuse reflection. It is mentioned in Section 3.1 that when both specular reflection and diffuse reflection exist and it can not be determined which reflection is dominant, there will be a $\frac{\pi}{2}$ -ambiguity between AoLP φ and azimuth angle ϕ . When the azimuth difference of two adjacent pixels is tiny, specular reflection and diffuse reflection are dominant, respectively, the φ of the two pixels will differ by 90° , resulting in the discontinuity of the AoLP map shown in Fig.2.

The intrinsic fault in the AoLP map of the transparent object is exploited to define the concept of **Physics-based Prior Confidence**. We first define the distance $d_{K,m}(i, j)$ between the pixels in the $K \times K$ neighborhood of point (i, j) and the average value:

$$d_{K,m}(i, j) = \sum_{p \in P_{i,j}} |p - \bar{p}_{i,j}|^m \quad (5)$$

where $P_{i,j}$ represents the set of pixel values in the $K \times K$ neighborhood of point (i, j) , $\bar{p}_{i,j}$ is the mean of pixel values belonging to the set $P_{i,j}$ and m is the smoothing exponential term. In this paper, K and m are set to 9, 0.5, respectively. By normalizing the distance map, the physics-based prior confidence can be obtained:

$$Confidence_{K,m}(i, j) = \frac{d_{K,m}(i, j)}{\max_{\substack{0 \leq x < W \\ 0 \leq y < H}} d_{K,m}(x, y)} \quad (6)$$

where H, W are the height and width of the AoLP map respectively. The physics-based prior confidence defined by the Eq.5 and Eq.6 is shown in the right picture in Fig.2. In fact, the physics-based prior confidence defined by the above equation is not only low in the area with high transmittance, but also at the junction of 0° and 180° in the AoLP map. According to the Eq.1, the AoLPs of 0° and 180° are physically consistent since the period of the sinusoid function is π , but there will be value jumps in the AoLP map resulting in low physics-based prior confidence. This situation is allowed because the higher confidence of the physics-based prior in such area will increase the adverse effect of π -ambiguity.

We input the physics-based prior confidence map as prior attention map into the network and guide the fusion of original-polar and physics-based prior at multiple levels to minimize error due to intrinsic faults of transparent SfP.

3.3 Network Architecture

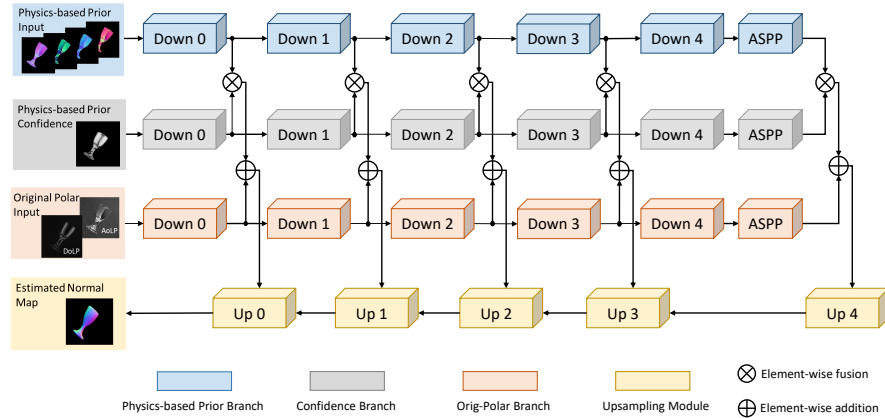


Fig. 3. Overview of our network architecture. Our network has three encoders and one decoder. The confidence branch is used to weight physics-based prior

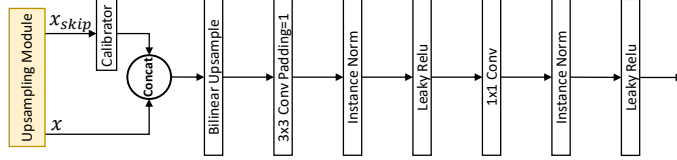


Fig. 4. Detailed structure of upsampling module

A straightforward way to use deep learning to solve the SfP problem is to input the original polarization images into the network for normal estimation, but it has been experimentally proven that directly inputting the original images will lead to high angular error and undesired lighting artifacts[3]. In order to overcome this problem, some works[3, 55] concatenates the physics-based prior with the original polarization images as network input. For the problem of transparent SfP, the confidence defined in Section 3.2 needs to be introduced into the network to alleviate the detrimental effects of physics-based prior reliability degradation. Different from the approach of concatenating the physics-based prior and the original polarization images, we regard it as a multi-modal fusion problem, using separate encoders to extract features of the two inputs. Features from two different inputs are fused at multiple levels according to the output of confidence branch, and finally, a decoder is employed to complete the normal estimation.

As shown in Fig.3, our network consists of three encoders and one decoder. The encoders are the physical prior branch, the physics-based prior confidence branch and the original polarization branch respectively. The structures of the encoders are completely the same, but the parameters are independent of each other. EPSANet50(Small) is adopted as the backbone of the Encoder, which is an improved backbone that replaces the Bottleneck in ResNet50 by ESPANet Block which exploits channel attention mechanism[51]. Before the Encoder, the module named ‘Down 0’ consisting of a 1×1 convolutional layer and a BatchNorm layer is used to force the network to extract the per-pixel feature. At the end of the Encoder, we add an ASPP(Atrous Spatial Pyramid Pooling) module to enhance the network’s ability to capture multi-scale information[6]. The features of the five levels of the three encoders x_{orig} , x_c , x_{prior} are extracted and fused, i.e. the element-wise fusion in Fig.3:

$$x_{fusion} = x_{orig} + \text{Sigmoid}(x_c) \cdot x_{prior} \quad (7)$$

where $\text{Sigmoid}(\cdot)$ is used to convert x_c into probabilities. Then, the U-Net style skip connection[36] is employed to introduce the fused features of different levels into the upsampling modules.

The detailed structure of the upsampling module is shown in Fig.4. The calibrator connected after the skip input is used to adjust the number of channels and size of the skip connection, and its structure is consistent with the main structure of the upsampling module. The main structure consists of two convolu-

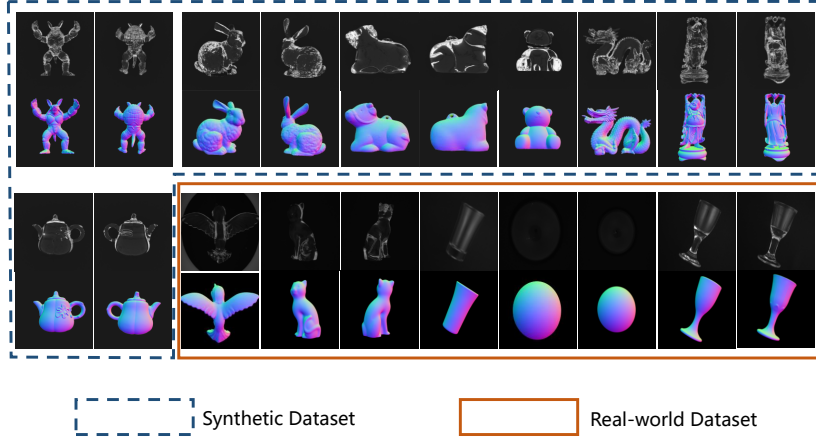


Fig. 5. TransSfP Dataset. TransSfP dataset consists of two parts: synthetic dataset and real-world dataset. The synthetic dataset consists of 936 samples of 13 objects (including the front and back of the same object) at different angles. The real dataset consists of 486 samples of 10 objects at different angles. Only some objects are listed in this figure

tional layers: a 3×3 convolutional layer with padding 1 and a 1×1 convolutional layer that is used to adjust the number of channels of the output feature map to the specified value.

Lastly, the cosine similarity commonly used in normal estimation is employed as the loss function of our network.

$$L = \sum_{i=0}^W \sum_{j=0}^H \left(1 - \frac{N_{i,j} \cdot \hat{N}_{i,j}}{\|N_{i,j}\|_2 \|\hat{N}_{i,j}\|_2} \right) \quad (8)$$

where $N_{i,j}$ represents the ground-truth normal vector at the location (i, j) , and $\hat{N}_{i,j}$ is the estimated normal vector.

3.4 TransSfP Dataset

We establish the TransSfP dataset for transparent shape from polarization, which contains raw polarization images, physical prior normal maps and ground-truth normal maps. TransSfP consists of two parts as shown in Fig.5: the real-world dataset and synthetic dataset.

Fig.6 is our setup for acquiring the TransSfP dataset. A simple optical difuser[24] is used to simulate global illumination so that transparent surfaces have uniform reflections in all directions. A DLASA G3-GM14-M2450 polarization camera that uses Sony IMX250MZR Mono sensor[35] is employed as our capture

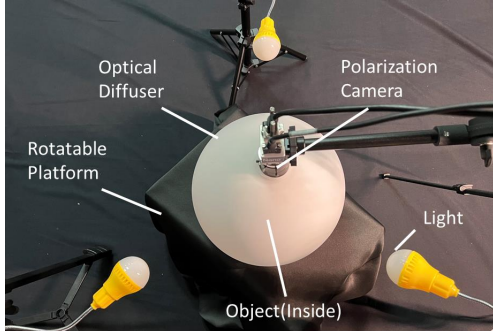


Fig. 6. Setup for acquiring real-world TransSfP dataset

device, which can capture four polarization images(at θ_{pol} of $0^\circ, 45^\circ, 90^\circ, 135^\circ$) at a single shot. We coat transparent objects with powder and reconstructed their 3D models by using a 3D scanner with an accuracy of $0.1mm$, and then manually align them with the captured polarization images in the unity game engine to obtain the ground-truth normal maps. Using the above steps, we build the real-world dataset of 10 different objects, each of which is rotated between 0° and 360° at 5° - 10° intervals, resulting in a total of 486 samples.

The synthetic dataset is created since the real-world data acquisition requires manual alignment, resulting in the difficulty of acquiring enough real-world data for training. We establish a scene similar to the setup in Fig.6 and implement an integrator capable of outputting a camera-space normal map in the mitsuba2[33], a physical render that can track the full polarization state of light during a simulation. The 3D models of 13 objects, collected from DiLiGenT-MV dataset[19] and Stanford 3D Scanning Repository[18], are placed in the scene we build to run polarization rendering. Each object is rotated 72 times from 0° to 360° , resulting in a total of 936 samples in the synthetic dataset.

3.5 Implementation Details

We implement our model on PyTorch and the model is trained on an NVIDIA GeForce RTX 3090 GPU(24GB) with batch size of 6. The Adam optimizer[15] with an initial learning rate of $1e-6$ and a weight decay coefficient of $5e-4$ is used for optimizing the network. We adopt the Step learning rate decreasing strategy, the learning rate times 0.1 every 9 epochs. To reduce memory usage, we crop the images to 512×512 patches in the data augmentation stage.

4 Experiments

4.1 Experimental Setup

We use the evaluation metrics commonly used in normal estimation, including mean angular error(*mean,MAE*), median angular error(*median*) and Accuracy 11.25° , 22.5° , 30° , which represent the ratio of the number of pixels with an error lower than this value to the total number of valid pixels. All samples in the TransSfP synthetic dataset are used for training, and some objects in the real-world dataset are also employed for training to make up for the difference between the synthetic dataset and the real-world dataset.

4.2 Comparisons to Baselines

We employ two physics-based SfP methods, Miyazaki et al.[28], Mahmoud et al.[23], and three learning-based methods, DeepSfP[3], Kondo et al.[16], SfP in the Wild(SPW)[17], as the baselines of our method. Where the learning-based methods' codes are not publicly accessible, we implemented the three models and retrained them on our TransSfP dataset. Mahmoud's method needs to provide albedo and light source direction, we assume the albedo is uniform of 1, and the light source direction is estimated using the method proposed by Smith et al.[40]. Fig.7 is a visual display of the comparison with baselines, Table 1

Table 1. Our method achieves the best results for each object in the test set. The best results in the table is marked in **Bold**

Method	Mean Angular Error ↓							
	Hemi-Sph -Big	Hemi-Sph -Small	Bird	Cat-Back	Cat-Front	Tiny-Cup	Tiny-Cup -Edges	All
Miyazaki	36.11°	36.35°	62.38°	64.40°	65.79°	70.49°	90.17°	55.62°
Mahmoud	68.57°	68.20°	66.98°	70.04°	69.30°	72.16°	65.89°	68.72°
DeepSfP	13.18°	14.42°	28.42°	20.02°	22.15°	15.88°	18.94°	19.00°
SPW	13.48°	12.87°	31.86°	21.85°	24.59°	15.28°	18.86°	19.83°
Kondo	24.61°	20.46°	27.24°	19.93°	20.32°	17.03°	20.11°	21.39°
Ours	9.40°	10.91°	25.04°	19.22°	19.90°	15.25°	17.34°	16.72°

lists the quantitative results of the comparison. Our method achieves the best performance on all objects in the test set, and our MAE is reduced by 2.3° compared to DeepSfP, the method closest to ours, especially for hemispherical objects. It can be seen from Fig.7 that the normal estimations of DeepSfP are too smooth and lose detailed information, especially the estimations of hemispherical objects basically have the same direction, which is the reason why the Accuracy 22.5° and Accuracy 30° of DeepSfP in Table 3 are closer to ours than Accuracy 11.25° .

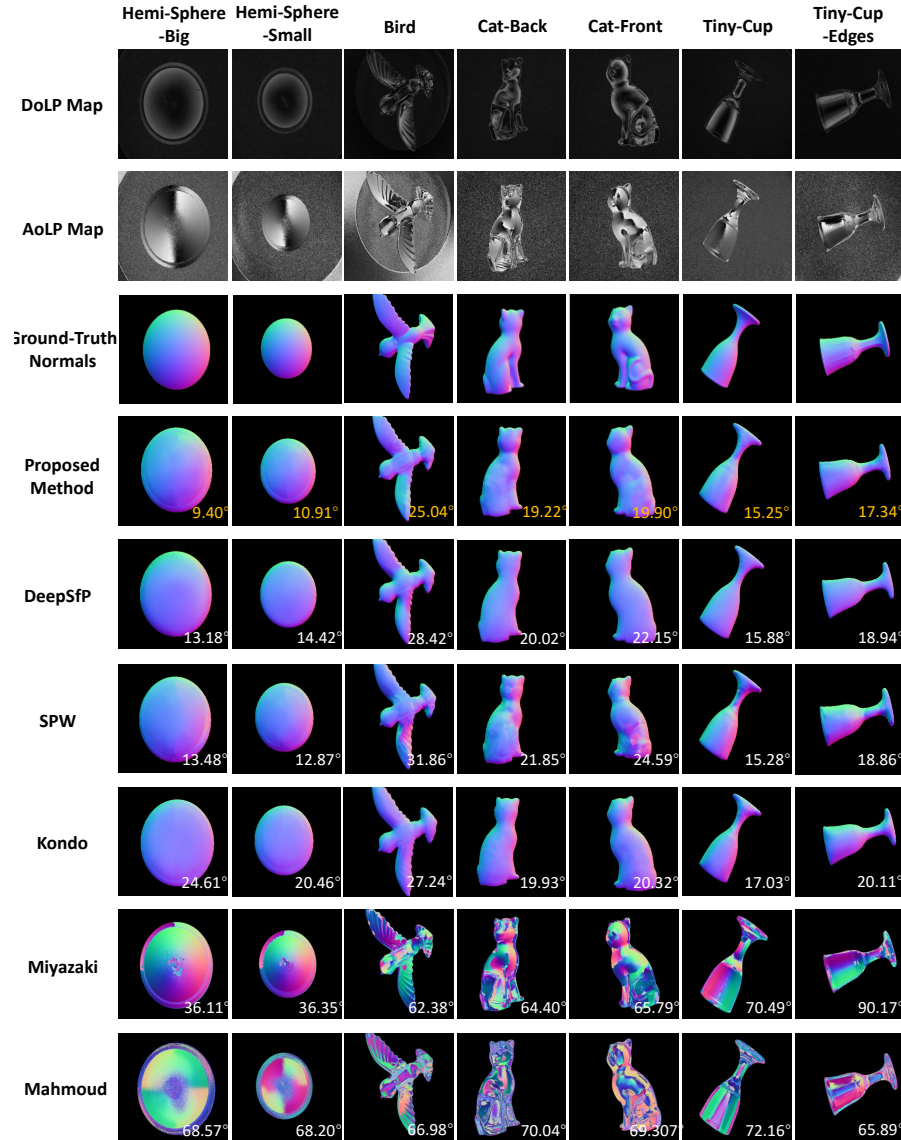


Fig. 7. Comparison of our method with baselines. Our method achieves the best results on test objects than other learning-based methods and is more effective on hemispherical objects since they are more susceptible to background transmission

4.3 Importance of Physics-based Prior Confidence

Table 2. Ablation experiment results on prior confidence

Confidence	Mean Angular Error ↓							
	Hemi-Sph -Big	Hemi-Sph -Small	Bird	Cat-Back	Cat-Front	Tiny-Cup -Edges	All	
Ours without x_c	14.22°	15.41°	23.09°	18.29°	19.92°	15.59°	18.09°	17.80°
Ours with x_c	9.40°	10.92°	25.05°	19.23°	19.90°	15.25°	17.34°	16.73°

We perform the ablation experiment to verify the importance of our proposed physics-based prior confidence. We set x_c to constant 1 to remove the confidence branch in the fusion module and other experimental settings are kept. The quantitative results of the ablation experiment are presented in Table 2. To better illustrate the importance of prior confidence, we list the results of different objects in the test set. After supplementing the prior confidence map, the improvement of hemispherical objects is the most obvious. Fig.8 shows the error maps before and after supplementing the prior confidence map to Hemi-Sphere-Big. The areas with lower confidence have lower angular error.

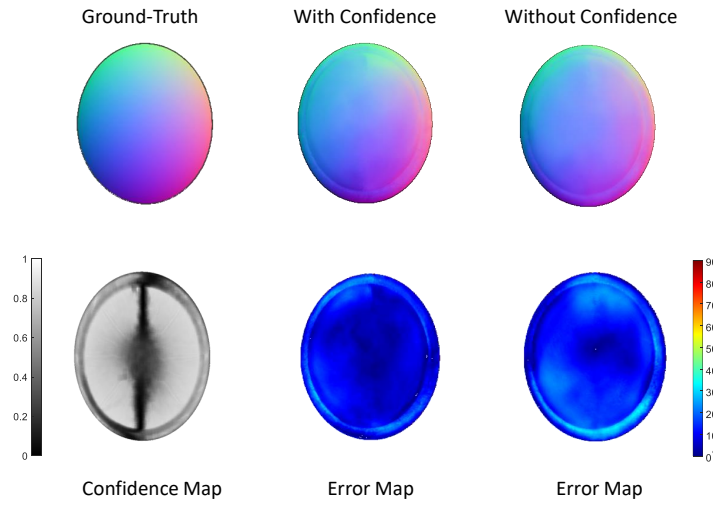


Fig. 8. Importance of prior confidence. After supplementing prior confidence, the angular error of the area with a low confidence value is reduced

It is noted that the angular error decreases after removing the confidence on Bird and Cat-Back. The surface of these objects is more complex, which leads to a low level of prior confidence in most areas, resulting in the overall lower dependence on the physical prior.

4.4 Comparisons of Network Architectures

Table 3. Comparison of network architectures

Network	Angular Error ↓		Accuracy ↑		
	Mean	Median	11.25°	22.5°	30°
U-Net	25.20°	22.90°	16.06%	49.42%	69.07%
PS-FCN	25.93°	22.42°	22.06%	52.79%	71.12%
DeepLabV3+	21.90°	18.93°	21.04%	63.78%	81.84%
DeepSfP	19.00°	14.91°	38.36%	77.36%	87.48%
SPW	21.73°	18.43°	28.38%	61.24%	84.00%
Kondo	24.40°	22.20°	18.95%	54.39%	75.09%
Ours	16.72°	13.36°	45.51%	78.86%	89.98%

Our network uses the fusion architecture of Multi-Encoders-Single-Decoder as shown in Fig.3. To illustrate the effectiveness of our architecture, we conduct the comparison with several commonly used semantic segmentations networks such as U-Net[36], DeepLabV3+[6] and models for normal estimation, PS-FCN[5], DeepSfP[3], SPW[17], Kondo[16]. All networks have the same inputs, including the orig-polar input, physics-based prior input and transmission confidence map. The quantitative results in Table 3 show that our architecture achieves the best performance on all metrics. The original polarization information and the physics-based prior are converted through Frenel’s physical model, hence they can be regarded as different levels of polarization information. Direct concatenates will destroy the relationship between different levels. The experimental results prove that our considering of treating them as different levels of information and then transforming it into a multimodal fusion problem is effective.

5 Conclusions

In this paper, we present the network designed for transparent shape from polarization. The network is quantitatively validated on the TransSfP dataset, the first dataset for transparent SfP. To reduce the angular error caused by physics-based prior degradation of transparent objects, we utilize the intrinsic fault of the AoLP map to define the concept of physics-based prior confidence and use a multi-modal network architecture to fuse the orig-polar input and physics-based

prior input. Experimental results illustrate that our method achieves the best results on all objects in the test set.

We noticed that the prior confidence does not have a positive effect on all test objects, which is a limitation of our work and this problem is left to our future work. In addition, the intrinsic fault of pure SfP information limits the accuracy of transparent shape estimation. How to blender SfP information with other sensors' to improve the estimation accuracy of transparent shape is also one of our future research directions.

References

1. Atkinson, G.A., Hancock, E.R.: Recovery of surface orientation from diffuse polarization. *IEEE transactions on image processing* **15**(6), 1653–1664 (2006)
2. Ba, Y., Chen, R., Wang, Y., Yan, L., Shi, B., Kadambi, A.: Physics-based neural networks for shape from polarization (2019)
3. Ba, Y., Gilbert, A., Wang, F., Yang, J., Chen, R., Wang, Y., Yan, L., Shi, B., Kadambi, A.: Deep shape from polarization. In: European Conference on Computer Vision. pp. 554–571. Springer (2020)
4. Basri, R., Jacobs, D., Kemelmacher, I.: Photometric stereo with general, unknown lighting. *International Journal of computer vision* **72**(3), 239–257 (2007)
5. Chen, G., Han, K., Wong, K.Y.K.: Ps-fcn: A flexible learning framework for photometric stereo. In: Proceedings of the European conference on computer vision (ECCV). pp. 3–18 (2018)
6. Chen, L.C., Zhu, Y., Papandreou, G., Schroff, F., Adam, H.: Encoder-decoder with atrous separable convolution for semantic image segmentation. In: Proceedings of the European conference on computer vision (ECCV). pp. 801–818 (2018)
7. Cui, Z., Gu, J., Shi, B., Tan, P., Kautz, J.: Polarimetric multi-view stereo. In: Proceedings of the IEEE conference on computer vision and pattern recognition. pp. 1558–1567 (2017)
8. Deschaintre, V., Lin, Y., Ghosh, A.: Deep polarization imaging for 3d shape and svbrdf acquisition. In: Proceedings of the IEEE/CVF Conference on Computer Vision and Pattern Recognition. pp. 15567–15576 (2021)
9. Eren, G., Aubreton, O., Meriaudeau, F., Secades, L.S., Fofi, D., Naskali, A.T., Truchetet, F., Ercil, A.: Scanning from heating: 3d shape estimation of transparent objects from local surface heating. *Optics express* **17**(14), 11457–11468 (2009)
10. Fang, H., Fang, H.S., Xu, S., Lu, C.: Transcg: A large-scale real-world dataset for transparent object depth completion and grasping. *arXiv preprint arXiv:2202.08471* (2022)
11. Fukao, Y., Kawahara, R., Nobuhara, S., Nishino, K.: Polarimetric normal stereo. In: Proceedings of the IEEE/CVF Conference on Computer Vision and Pattern Recognition. pp. 682–690 (2021)
12. Horn, B.K.: Shape from shading: A method for obtaining the shape of a smooth opaque object from one view (1970)
13. Kadambi, A., Taamazyan, V., Shi, B., Raskar, R.: Polarized 3d: High-quality depth sensing with polarization cues. In: Proceedings of the IEEE International Conference on Computer Vision. pp. 3370–3378 (2015)
14. Kadambi, A., Taamazyan, V., Shi, B., Raskar, R.: Depth sensing using geometrically constrained polarization normals. *International Journal of Computer Vision* **125**(1), 34–51 (2017)

15. Kingma, D.P., Ba, J.: Adam: A method for stochastic optimization. arXiv preprint arXiv:1412.6980 (2014)
16. Kondo, Y., Ono, T., Sun, L., Hirasawa, Y., Murayama, J.: Accurate polarimetric brdf for real polarization scene rendering. In: European Conference on Computer Vision. pp. 220–236. Springer (2020)
17. Lei, C., Qi, C., Xie, J., Fan, N., Koltun, V., Chen, Q.: Shape from polarization for complex scenes in the wild. arXiv preprint arXiv:2112.11377 (2021)
18. Levoy, M., Gerth, J., Curless, B., Pull, K.: The stanford 3d scanning repository. URL <http://www-graphics.stanford.edu/data/3dscanrep> 5(10) (2005)
19. Li, M., Zhou, Z., Wu, Z., Shi, B., Diao, C., Tan, P.: Multi-view photometric stereo: A robust solution and benchmark dataset for spatially varying isotropic materials. *IEEE Transactions on Image Processing* **29**, 4159–4173 (2020)
20. Li, Z., Yeh, Y.Y., Chandraker, M.: Through the looking glass: Neural 3d reconstruction of transparent shapes. In: Proceedings of the IEEE/CVF Conference on Computer Vision and Pattern Recognition. pp. 1262–1271 (2020)
21. Liu, D., Chen, X., Yang, Y.H.: Frequency-based 3d reconstruction of transparent and specular objects. In: Proceedings of the IEEE Conference on Computer Vision and Pattern Recognition. pp. 660–667 (2014)
22. Liu, J., Lu, X., Jin, W., Wang, X., Qiu, S., Wen, R.: Transparent surface orientation from polarization imaging using vector operation. *Applied Optics* **57**(9), 2306–2313 (2018)
23. Mahmoud, A.H., El-Melegy, M.T., Farag, A.A.: Direct method for shape recovery from polarization and shading. In: 2012 19th IEEE International Conference on Image Processing. pp. 1769–1772. IEEE (2012)
24. Miyazaki, D., Ikeuchi, K.: Inverse polarization raytracing: estimating surface shapes of transparent objects. In: 2005 IEEE Computer Society Conference on Computer Vision and Pattern Recognition (CVPR’05). vol. 2, pp. 910–917. IEEE (2005)
25. Miyazaki, D., Ikeuchi, K.: Shape estimation of transparent objects by using inverse polarization ray tracing. *IEEE Transactions on Pattern Analysis and Machine Intelligence* **29**(11), 2018–2030 (2007)
26. Miyazaki, D., Kagesawa, M., Ikeuchi, K.: Determining shapes of transparent objects from two polarization images. In: MVA. pp. 26–31 (2002)
27. Miyazaki, D., Kagesawa, M., Ikeuchi, K.: Transparent surface modeling from a pair of polarization images. *IEEE Transactions on Pattern Analysis and Machine Intelligence* **26**(1), 73–82 (2004)
28. Miyazaki, D., Tan, R.T., Hara, K., Ikeuchi, K.: Polarization-based inverse rendering from a single view. In: Computer Vision, IEEE International Conference on. vol. 3, pp. 982–982. IEEE Computer Society (2003)
29. Morel, O., Ferraton, M., Stolz, C., Gorria, P.: Active lighting applied to shape from polarization. In: 2006 International Conference on Image Processing. pp. 2181–2184. IEEE (2006)
30. Morel, O., Meriaudeau, F., Stolz, C., Gorria, P.: Polarization imaging applied to 3d reconstruction of specular metallic surfaces. In: Machine Vision Applications in Industrial Inspection XIII. vol. 5679, pp. 178–186. International Society for Optics and Photonics (2005)
31. Morel, O., Stolz, C., Meriaudeau, F., Gorria, P.: Active lighting applied to three-dimensional reconstruction of specular metallic surfaces by polarization imaging. *Applied optics* **45**(17), 4062–4068 (2006)

32. Morris, N.J., Kutulakos, K.N.: Reconstructing the surface of inhomogeneous transparent scenes by scatter-trace photography. In: 2007 IEEE 11th International Conference on Computer Vision. pp. 1–8. IEEE (2007)
33. Nimier-David, M., Vicini, D., Zeltner, T., Jakob, W.: Mitsuba 2: A retargetable forward and inverse renderer. ACM Transactions on Graphics (TOG) **38**(6), 1–17 (2019)
34. Ohta, J.: Smart CMOS image sensors and applications. CRC press (2017)
35. Rebhan, D., Rosenberger, M., Notni, G.: Principle investigations on polarization image sensors. In: Photonics and Education in Measurement Science 2019. vol. 11144, p. 111440A. International Society for Optics and Photonics (2019)
36. Ronneberger, O., Fischer, P., Brox, T.: U-net: Convolutional networks for biomedical image segmentation. In: International Conference on Medical image computing and computer-assisted intervention. pp. 234–241. Springer (2015)
37. Saito, M., Sato, Y., Ikeuchi, K., Kashiwagi, H.: Measurement of surface orientations of transparent objects by use of polarization in highlight. JOSA A **16**(9), 2286–2293 (1999)
38. Sajjan, S., Moore, M., Pan, M., Nagaraja, G., Lee, J., Zeng, A., Song, S.: Clear grasp: 3d shape estimation of transparent objects for manipulation. In: 2020 IEEE International Conference on Robotics and Automation (ICRA). pp. 3634–3642. IEEE (2020)
39. Shi, B., Yang, J., Chen, J., Zhang, R., Chen, R.: Recent progress in shape from polarization. Advances in Photometric 3D-Reconstruction pp. 177–203 (2020)
40. Smith, W.A., Ramamoorthi, R., Tozza, S.: Height-from-polarisation with unknown lighting or albedo. IEEE transactions on pattern analysis and machine intelligence **41**(12), 2875–2888 (2018)
41. Tanaka, K., Mukaigawa, Y., Kubo, H., Matsushita, Y., Yagi, Y.: Recovering transparent shape from time-of-flight distortion. In: Proceedings of the IEEE Conference on Computer Vision and Pattern Recognition. pp. 4387–4395 (2016)
42. Tang, Y., Chen, J., Yang, Z., Lin, Z., Li, Q., Liu, W.: Depthgrasp: Depth completion of transparent objects using self-attentive adversarial network with spectral residual for grasping. In: 2021 IEEE/RSJ International Conference on Intelligent Robots and Systems (IROS). pp. 5710–5716. IEEE (2021)
43. Tian, X., Liu, R., Wang, Z., Ma, J.: High quality 3d reconstruction based on fusion of polarization imaging and binocular stereo vision. Information Fusion **77**, 19–28 (2022)
44. Vedel, M., Lechocinski, N., Breugnot, S.: 3d shape reconstruction of optical element using polarization. In: Polarization: Measurement, Analysis, and Remote Sensing IX. vol. 7672, pp. 21–33. SPIE (2010)
45. Wetzstein, G., Roodnick, D., Heidrich, W., Raskar, R.: Refractive shape from light field distortion. In: 2011 International Conference on Computer Vision. pp. 1180–1186. IEEE (2011)
46. Wolff, L.B., Boult, T.E.: Constraining object features using a polarization reflectance model. Phys. Based Vis. Princ. Pract. Radiom **1**, 167 (1993)
47. Wu, B., Zhou, Y., Qian, Y., Gong, M., Huang, H.: Full 3d reconstruction of transparent objects. arXiv preprint arXiv:1805.03482 (2018)
48. Yang, L., Tan, F., Li, A., Cui, Z., Furukawa, Y., Tan, P.: Polarimetric dense monocular slam. In: Proceedings of the IEEE conference on computer vision and pattern recognition. pp. 3857–3866 (2018)
49. Yeung, S.K., Wu, T.P., Tang, C.K., Chan, T.F., Osher, S.: Adequate reconstruction of transparent objects on a shoestring budget. In: CVPR 2011. pp. 2513–2520. IEEE (2011)

50. Yeung, S.K., Wu, T.P., Tang, C.K., Chan, T.F., Osher, S.J.: Normal estimation of a transparent object using a video. *IEEE Transactions on Pattern Analysis and Machine Intelligence* **37**(4), 890–897 (2014)
51. Zhang, H., Zu, K., Lu, J., Zou, Y., Meng, D.: Epsanet: An efficient pyramid squeeze attention block on convolutional neural network. *arXiv preprint arXiv:2105.14447* (2021)
52. Zhu, D., Smith, W.A.: Depth from a polarisation+rgb stereo pair. In: *Proceedings of the IEEE/CVF Conference on Computer Vision and Pattern Recognition*. pp. 7586–7595 (2019)
53. Zhu, L., Mousavian, A., Xiang, Y., Mazhar, H., van Eenbergen, J., Debnath, S., Fox, D.: Rgb-d local implicit function for depth completion of transparent objects. In: *Proceedings of the IEEE/CVF Conference on Computer Vision and Pattern Recognition*. pp. 4649–4658 (2021)
54. Zhu, Y., Qiu, J., Ren, B.: Transfusion: A novel slam method focused on transparent objects. In: *Proceedings of the IEEE/CVF International Conference on Computer Vision*. pp. 6019–6028 (2021)
55. Zou, S., Zuo, X., Qian, Y., Wang, S., Xu, C., Gong, M., Cheng, L.: 3d human shape reconstruction from a polarization image. In: *European Conference on Computer Vision*. pp. 351–368. Springer (2020)
56. Zou, S., Zuo, X., Wang, S., Qian, Y., Guo, C., Ji, W., Li, J., Gong, M., Cheng, L.: Human pose and shape estimation from single polarization images. *arXiv preprint arXiv:2108.06834* (2021)